Comput Mech
DOI 10.1007/s00466-012-0751-5

ORIGINAL PAPER

Oblique mid ocean ridge subduction modelling with the parallel fast multipole boundary element method

L. Quevedo · B. Hansra · G. Morra · N. Butterworth · R. D. Müller

Received: 27 February 2012 / Accepted: 14 June 2012

Abstract Geodynamic models describe the thermo-mechanical evolution of rheologically intricate structures spanning different length scales, yet many of their most relevant dynamic features can be studied in terms of low Reynolds number multiphase creep flow of isoviscous and isopycnic structures. We use the BEM- EARTH code to study the interaction of the lithosphere and mantle within the solid earth system in this approximation. BEM- EARTH overcomes the limitations of traditional FD/FEM for this problem by considering only the dynamics of Boundary Integral Elements at fluid interfaces, and employing a parallel multipole solver accelerated with a hashed octtree. As an application example, we self-consistently model the processes controlling the subduction of an oblique mid-ocean ridge in a global 3D spherical setting in a variety of cases, and find a critical angle characterising the transition between an extensional strain regime related to tectonic plate necking and a compressive regime related to Earth curvature effects.

Keywords Boundary integral element · Mid ocean ridges · Subduction mechanics

L. Quevedo (✉) · B. Hansra · G. Morra · N. Butterworth · R. D. Müller
EarthByte Group, School of Geosciences, University of Sydney, Sydney, NSW 2006, Australia
e-mail: leonardo.quevedo@sydney.edu.au

G. Morra
School of Earth and Environmental Sciences, Seoul National University, Seoul, South Korea

1 Introduction

Subduction, the geological process by which the top brittle portion of the upper mantle (the lithosphere) sinks into the more ductile interior of the solid Earth, is the key geodynamic feature of our planet. Downwellings of cold and dense rocks at subduction zones provide the density, temperature and pressure gradients that drive mantle convection; generate the main force propelling plate tectonics (the *slab pull*); and are linked to most of the volcanism and seismicity that puts human lives at risk. The large body of research associated with subduction modelling attests to the complex geophysical aspects involved in its description as well as to difficulties arising from the scarcity of time and depth dependent observations relevant for their understanding.[1]

Multiphysics simulation has contributed to increase the degree of realism of subduction models by incorporating a broad range of attributes and processes influencing very general visco-elasto-plastic rock rheology depending on chemical composition, pressure, temperature and stress. Additionally, setting this systems in a planetary scale spanning very large variations in size and physical properties result in very complex models that push the traditional FEM and FD methods to their limit. Such immense and intricate parameter space makes extremely difficult to pinpoint the effect of an individual variable in the behaviour of the system. As a consequence, in order to discover parameters that control dynamic features of subduction, many systems have been explored only in 2D or in highly symmetric simplified 3D geometries, and with physical constrains to reduce the total number of degrees of freedom.

Global tectonic modes are particular examples in which the simplification leads to concise relationships between

[1] For a review on current trends in subduction modelling see [11].

Published online: 03 July 2012

input variables and dynamic behaviour. By describing the full solid earth convection flow in spherical harmonics, the global plate kinematic behaviour can be inferred starting from a simple rheological model of the mantle and an estimation of plate driving forces based on models of the subduction history [15,10]. In this way it has been possible to predict (or more precisely to reproduce) the observed present day and the reconstructed paleo plate kinematics from simplified models of the viscosity and density heterogeneities of the solid earth.

Recent models [1,5,6] have revealed the importance of slab pull variations due to the parallel subduction of a mid-ocean ridge (MOR) in tectonic dynamics. Since they define the regions where oceanic lithosphere is being created from the cooling of magma, these ridges tend to be hotter and more buoyant than the rest of the plate. As they approach a subduction trench that is parallel to their axis, they might cause necking and detachment of the portion that has already subducted (the *slab*) and eventually a dramatic decrease of slab pull which could lead to subduction cessation. Similarly, the subduction of an active ridge orthogonal to the trench could lead to the opening of a window between two slabs significantly altering the pattern of mantle flow in the solid earth. It is therefore essential to the understanding of global tectonics to consider the subduction of such ridges in the more general oblique setting in which they usually occur.

We present the first 3D self consistent dynamical simulations of oblique MOR subduction spanning the complete range of oblique collision angles. The self-consistent dynamic description of 3D ridges, modelled as an indentation in an otherwise flat rectangular tectonic plate, is simplified by assuming a temperature independent viscous creep rheology governed by the Stokes equation. Using a multipole accelerated boundary integral element method, we were able to explore the full range of values of different ridge-trench collision angles between the parallel and orthogonal cases, compare strain estimations on the ridge for different collision angles, and characterise the transition between an extensional regime associated to slab tearing and a compressive regime related to Earth curvature effects. Such transition was impossible to detect in previous works which were limited by computational complexity to the analysis of simplified geometries, end-member cases, 2D models, or particular regional studies [20].

For this study, we use the BEM- EARTH [17,18,21,24] geodynamic modelling software, which allows the study of regional subduction in the context of global spherical mantle flow, reducing the problem dimensionality and accelerating the solution of the resulting dense systems. By integrating multipole methods parallelised using MPI for distributed memory architectures with hashed octtree algorithms for fast identification of near and far-field interacting elements, BEM- EARTH is able to overcome some of the limitations of finite difference/element methods traditionally used in geodynamics.

2 MOR subduction

Despite recent advances, most geodynamic models of ridge-trench collision are two dimensional and involve either a parallel or an orthogonal ridge-axis-to-trench angle. Furthermore, ridge subduction beyond simple slab detachment in the parallel case, has not been reproduced by any 2D thermo-mechanical model and is believed to be caused by 3D effects.

Present day examples of ridge-transform systems intersecting convergent margins like the Chile (Nazca-Antarctica), Rivera (Rivera-Pacific) and Mendocino triple junctions [4] indicate that the simultaneous subduction of two adjacent plates along the same trench is not uncommon, and is manifested trough different tectonic settings for which the angle between the transform or ridge axis and the trench varies. Such ridge-trench collisions have been almost exclusively studied in the parallel case in relation to the the dynamics of subduction cessation and slab detachment [5,1,6] and in the orthogonal case, where they are related to the formation of slab windows [14]. In the parallel case, when a ridge approaches a convergent margin the downgoing material becomes progressively younger and harder to subduct. Lithosphere as old as 10 Myr is considered to be already neutrally buoyant with respect to the surrounding mantle [8] and is not expected to contribute significantly to the downward pull. Eventually, the combined effect of buoyancy and the weakening of the slab at the ridge axis may lead to the cessation of subduction and subsequent detachment of the subducted slab [5,12]. In the orthogonal case, as the diverging oceanic plates subduct, magma that could form at the edges of the plates will not be able to cool down to continue lithospheric formation, thereby forming a *slab window*. Such tearing of the slab and an eventual detachment inhibits the capacity of slabs to propagate stresses through plates and their boundaries and alter the pattern of mantle convection [9,10] therefore having a profound impact on the dynamics of plates and mantle [6,33]. Assuming slab pull is the most significant force driving plate tectonics, the decrease of the pull force associated with ridge subduction could have dramatic implications for tectonic dynamics, in particular for global plate reorganisations.

We use the BEM- EARTH software to self-consistently model the processes controlling such a tectonic setup in a variety of cases, assuming a lithosphere immersed in a less viscous and less dense mantle, an inviscid highly dense core and virtually frictionless plate boundaries.

3 Fluid mechanical model

Mantle circulation and plate tectonic dynamics in the solid earth, characterised by very low Reynolds number, is governed by the Stokes equation for steady, highly viscous flow

$$\nabla \cdot \sigma + \rho \mathbf{b} = 0. \tag{1}$$

where σ_{ij} is the full stress tensor, and $\mathbf{b}$ represents the body forces. In terms of the dynamic viscosity μ, the velocity field $\mathbf{u}$, and the pressure P, the gradient of the stress tensor is given by

$$\nabla \cdot \sigma = \mu \nabla^2 \mathbf{u} - \nabla P. \tag{2}$$

Following several numerical and experimental studies [3,25], we approximate the fluid dynamics of subduction by considering the mantle and the lithosphere as regions of homogeneous density and viscosity, disregarding other the chemical and rheological inhomogeneities. We further assume a simple temperature independent rheology for such multiphase flow, and model only the fundamental forces controlling the process, which we take to be: the buoyancy resulting from the different densities between the flow phases; the viscous drag that might hamper or assist plate motion; and the viscous resistance to bending and stretching.

For our applications we will be interested in the dynamics of subducting plates considered as isoviscous and isopycnic surfaces immersed in a homogeneous mantle. We will therefore solve the flow field for a system consisting of an interface S_1 representing the surface of the earth, surrounded by an unbounded fluid and having disconnected closed interfaces inside representing the subducting slab S_3 and the core-mantle boundary S_2 (see Fig. 1). The boundary conditions are prescribed by the interfacial surface forces $\Delta\mathbf{f}$ resulting from the different material properties of each phase. From Eq. (1) we see that the normal stress discontinuity produced by the differential density ($\Delta\rho = \rho_2 - \rho_1$) of two phases subject to a gravitational acceleration $\mathbf{g}$, is

$$\Delta\mathbf{f}(\mathbf{x}) = \Delta\rho(\mathbf{x})\ (\mathbf{g}(\mathbf{x}) \cdot \mathbf{x})\ \mathbf{n}, \tag{3}$$

whereas the velocity field is continuous throughout the full domain. The gravitational acceleration inside the mantle varies in magnitude from $10.8\,\mathrm{ms}^{-2}$ at the core mantle boundary down to $9.8\,\mathrm{ms}^{-2}$ near the surface [31]. Given that main contributions to (3) come from the density contrast and the position, we will assume a radially oriented gravitational field of constant magnitude $g = 10\,\mathrm{ms}^{-2}$. Forcing, deformation and velocity fields are further required to vanish at infinity.

For a point $\mathbf{x}_0$ inside a region V where the viscosity μ is homogeneous, Eq. (1) can be solved for the flow field $\mathbf{u}(\mathbf{x})$ and the pressure field $P(\mathbf{x})$ using the Green function method. The boundary integral formulation [23] of the solution in terms of the Lagrangian specification of the flow field takes the form:

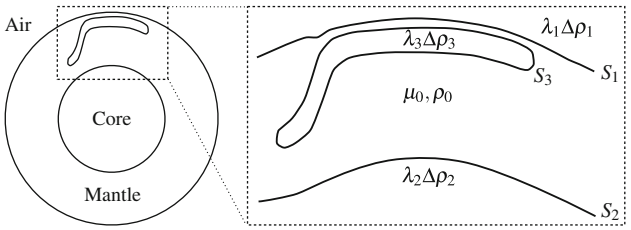

Fig. 1 Subducting plate dynamic as a multiphase flow bounded by the free surfaces S_i. S_1 represents the surface of the Earth, S_2 a viscosity transition at the core–mantle-boundary and S_3 the surface of the subducting plate

$$u_j(\mathbf{x}_0) = -\frac{1}{8\pi\mu}\int_{\partial V} f_i(\mathbf{x}) G_{ij}(\mathbf{x}, \mathbf{x}_0) dS(\mathbf{x}) + \frac{1}{8\pi}\int_{\partial V} u_i(\mathbf{x}) n_k(\mathbf{x}) T_{ijk}(\mathbf{x}, \mathbf{x}_0) dS(\mathbf{x}). \tag{4}$$

Here the cartesian components of the field $\mathbf{u}(\mathbf{x}) = u_j(\mathbf{x})\hat{\mathbf{e}}_j$ are represented in terms of the surface force $\mathbf{f} = \sigma \cdot \mathbf{n}$ and the fundamental solutions G_{ij} and T_{ijk} for the velocity and traction. The integral domain is the boundary ∂V of the region, where the surface element and the components of the normal are $dS(\mathbf{x})$ and $n_k(\mathbf{x})$ respectively. The explicit form of the fundamental solutions, known as *Stokeslet* and *Stresslet* are

$$G_{ij}(\mathbf{x}, \mathbf{x}_0) = \frac{\delta_{ij}}{r} + \frac{r_i r_j}{r^3}, \qquad T_{ijk}(\mathbf{x}, \mathbf{x}_0) = -6\frac{r_i r_j r_k}{r^5}, \tag{5}$$

where $\mathbf{r} = \mathbf{x} - \mathbf{x}_0$ and $r = |\mathbf{r}|$. The pressure field can be directly calculated through an integral equation analogous to (4) [23, Eq. (2.3.17)], yet we will only focus on the flow field since it completely defines the dynamic of the system.

In order to solve for the velocities using (4), we first need to find its values on the boundary given the particular constrain. To this aim, we first find the solution right on the boundary $\mathbf{x}_0 \in \partial V$, which leads the following expression involving the *principal value* (PV) of the Stresslet integral:

$$u_j(\mathbf{x}_0) = -\frac{1}{4\pi\mu}\int_{\partial V} f_i(\mathbf{x}) G_{ij}(\mathbf{x}, \mathbf{x}_0) dS(\mathbf{x}) + \frac{1}{4\pi}\overset{\mathrm{PV}}{\int_{\partial V}} u_i(\mathbf{x}) n_k(\mathbf{x}) T_{ijk}(\mathbf{x}, \mathbf{x}_0) dS(\mathbf{x}), \tag{6}$$

here the PV is the improper integral value when the point $\mathbf{x}_0$ is right on the boundary.

In practice, we will find the values for the velocity on the quasi-steady boundaries of multiphase flows for which we prescribe the known surface force $\mathbf{f} = \Delta\mathbf{f}$ that accounts for buoyancy.

Using mantle viscosity (density) μ_0 (ρ_0) as a reference and defining a relative viscosity $\lambda_i = \mu_i/\mu_0$ for each particular phase i, we can write the velocity at the boundary $S_i = \partial V_i$ of such phase as a Fredholm integral of the second kind [23,17,16]:

$$\mathbf{u}(\mathbf{x}_0) = -\left(\frac{1}{1+\lambda_i}\right)\frac{1}{4\pi\mu_0}\sum_j \int_{S_j} \mathsf{G}(\mathbf{x})\cdot\Delta\mathbf{f}(\mathbf{x})\,dS(\mathbf{x}),$$
$$-\sum_j \left(\frac{1-\lambda_j}{1+\lambda_i}\right)\frac{1}{4\pi}\overset{PV}{\int_{S_j}} \mathbf{u}(\mathbf{x})\cdot\mathsf{T}(\mathbf{x},\mathbf{x}_0)\cdot\mathbf{n}(\mathbf{x})\,dS(\mathbf{x}), \tag{7}$$

which might be solved using an iterative technique. Furthermore, we can study the evolution of the flow by solving only on the boundaries and use the Eq. (4) whenever we want a general solution at any point in space.

At each instant, the geometry of the interfaces completely defines the flow field. In turn, the flow field completely defines the evolution of the interfaces, which can be specified in terms of a set of Lagrangian points for each surface S_i:

$$\frac{\partial \mathbf{x}_{S_i}(t)}{\partial t} = \left[\mathbf{u}(\mathbf{x}_{S_i},t)\cdot\mathbf{n}\right]\mathbf{n} + \delta\mathbf{t}, \tag{8}$$

where $\mathbf{n}$ and $\mathbf{t}$ are unit vectors normal and tangential to the point at the surface and δ is a constant. Both the value of δ and the particular orientation of $\mathbf{t}$ are arbitrary. Since the surfaces S_i represent interfaces between fluids and tangential motion have no effect on their shape, we are free to choose $\delta\mathbf{t} = \mathbf{u}\cdot(\mathbf{1}-\mathbf{nn})$ and identify the velocity of points $\mathbf{x}_{S_i}$ with the velocity of the fluid,

$$\frac{\partial \mathbf{x}_{S_i}(t)}{\partial t} = \mathbf{u}(\mathbf{x}_{S_i},t), \tag{9}$$

which can be explicitly integrated numerically once the value of the flow field on the interface is known.

3.1 Thin lubrication layer

In self consistent simulations of tectonics involving only one plate, the negative buoyancy of the lithosphere would induce vertical sinking, since the mantle is free to overflow the surface of the plate. In order to simulate subduction behaviour without considering the contribution of surrounding plates or studying the global system of inter-plate stresses, we interpose a thin lubrication layer between the surface of the Earth and the surfaces contained within [17,22,25]. This layer allows the plate to slide in any tangential direction, but restores the isostatic equilibrium that keeps it from sinking radially.

4 Numerical method

We simulate the self-consistent fluid mechanical evolution of the subducting slab in a spherical setup, driven by buoyancy, viscous drag, and resistance to bending and stretching without kinematic constrains, using the BEM- EARTH code [17,18,21,24], a parallel multipole accelerated boundary integral element solver for the steady low Reynolds number flow.

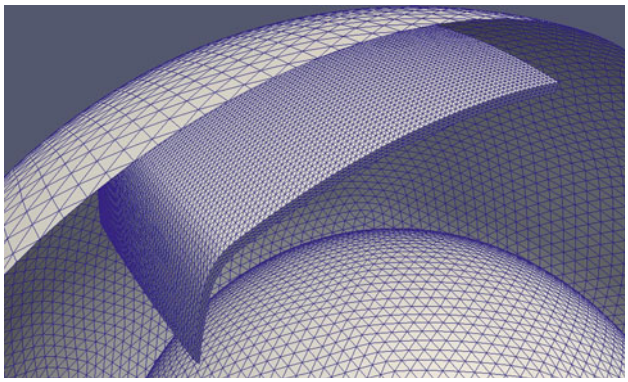

Fig. 2 Discretisation of a typical model of a subducting plate immersed in the mantle between the surface of the Earth and the core–mantle boundary

The boundary S_i of each phase is discretised in space as a 3D unstructured triangulated surface mesh (see Fig. 2) on which the variables ($\mathbf{u}, \mathbf{f}, \ldots$) are defined using the collocation approach. A local orthogonal cartesian coordinate system is used to represent the values of linear shape functions that interpolate the variables within each triangle. The kernels integrals in 7 are calculated analytically for this interpolation, leading to a numerically equivalent linear system of the form

$$\left[\Lambda + \mathsf{T}\right]\mathbf{U} = \mathbf{F}, \tag{10}$$

where Λ is a matrix containing constant coefficients associated with each surface relative viscosity, T is the discrete kernel of the Stresslet integral, $\mathbf{F}$ the numerical value of the Stokeslet integral on the surface and $\mathbf{U}$ the unknown velocities at each element.

Integrating the kernels to obtain the linear system (10) is a particularly complex task due to the presence of $\mathcal{O}(1/r^3)$ divergencies that render the integral hypersingular. The nature of the regularisation process required to obtain a closed form of the matrix elements [26] leads to very cumbersome expressions requiring the use of symbolic analytical computational tools.

As an example the Stokeslet term in (7) in terms of linear local shape functions $\varphi_a(\mathbf{x})$ defined at each triangle $\mathbf{x} \in T_a$ of the mesh, has the form

$$\sum_{a=1}^{N} g_a(\mathbf{x}_0) = \sum_{a=1}^{N}\int_{T_a} G_{ij}(\mathbf{x},\mathbf{x}_0)n_i(\mathbf{x})n_j(\mathbf{x}_0)\varphi_a(\mathbf{x})dS(\mathbf{x}), \tag{11}$$

where the integral is performed on each triangle. A closed expression for this integral in the local coordinate basis has the general form

$$g_a(\mathbf{x}_0) = n_i(\mathbf{x}) \left[\left(1 - \frac{y_0}{y}\right) A_{ij}(\mathbf{x}_0) - \frac{1}{y} B_{ij}(\mathbf{x}_0) \right] n_j(\mathbf{x}_0). \tag{12}$$

where A is a 3×3 matrix of rational functions, and B is a 3×3 matrix involving regular rational and trigonometric functions. The reader is referred to [26] for around 15 explicit independent terms present in each case: inside the triangle $\mathbf{x}_0 \in T_a$, outside the triangle $\mathbf{x}_0 \notin T_a$ and at the boundary of the triangle $\mathbf{x}_0 \in \partial T_a$.

4.1 Fast multipole acceleration

Equation (10) is well-conditioned but dense [34], meaning that the complexity of the calculation of the left hand side of Eq. (10) scales with N^2 for N boundary elements. The decay of the kernels in Eq. (5) and their derivatives with the distance may be used to overcome the poor scaling behaviour of a direct calculation by allowing the application of the fast multipole method [2,13]. In analogy with the multipole expansion of a potential outside the support of an electrostatic charge distribution, our kernels of interest are approximately degenerate, therefore the interaction between sufficiently separated points $\mathbf{x}$ and $\mathbf{y}$ can be approximated by an expression of the form

$$K(\mathbf{x} - \mathbf{y}) \approx \sum_{k=0}^{p-1} \Phi_k(\mathbf{x}) \Phi_k(\mathbf{y}) \tag{13}$$

Effectively decoupling the interactions and allowing a $\mathcal{O}(pN)$ complex calculation of sums of the form

$$\begin{aligned} &\sum_{i \neq j}^{N} V(\mathbf{x}_i) K(\mathbf{x}_i - \mathbf{x}_j) P(\mathbf{x}_j) \\ &\quad \approx \sum_{k=0}^{p-1} \left(\sum_{i=1}^{N} \Phi_k(\mathbf{x}_i) V(\mathbf{x}_i) \right) \Phi_k(\mathbf{x}_j) P(\mathbf{x}_j) \end{aligned} \tag{14}$$

in the Eq. (10). In our case the accelerated approximation algorithm is based on clustering the point-like triangle sources of stress and Stokes field at different length scales and integrate the interaction kernel according to their separation. When the points are close, the kernel is directly integrated, when they are far, the multipole expansion is used (see Fig. 3). BEM- EARTH implements multipole expansions for the Stokeslet or the Stresslet up to the second order.

The Stokeslet and Stresslet multipole expansion can be obtained from the degenerate approximation of the well known single-layer (point charge) and double-layer (dipole) electrostatic potentials [7,27]

$$\phi(\mathbf{x} - \mathbf{y}) = \frac{1}{|\mathbf{x} - \mathbf{y}|}, \qquad \Phi(\mathbf{x} - \mathbf{y}) = \frac{\mathbf{n} \cdot (\mathbf{x} - \mathbf{y})}{|\mathbf{x} - \mathbf{y}|^3}. \tag{15}$$

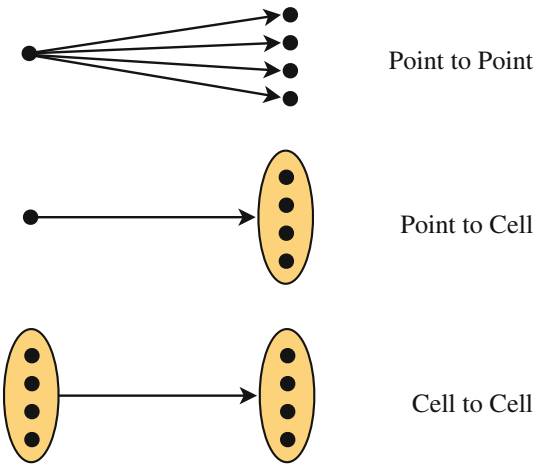

Fig. 3 Depending on the distance between the sources, the contribution to the interaction on each surface is done using local (point to point) or multipole terms (point to cell and cell to cell)

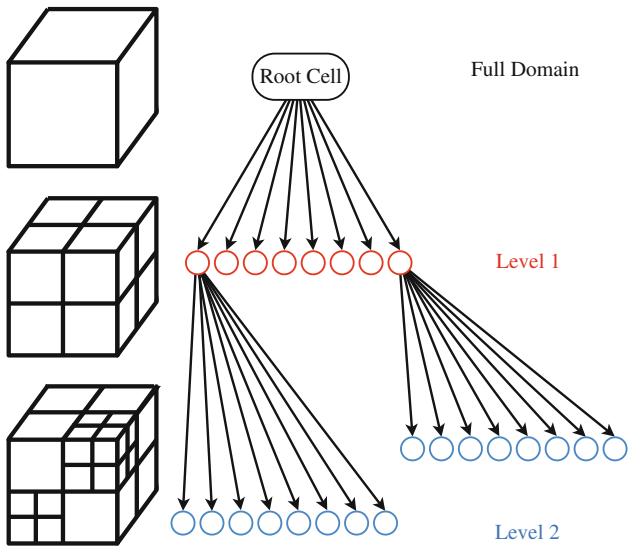

Fig. 4 A volume is progressively subdivided from the full *root cell* into finer regular partitions that define the cells at each level

Applying suitable generating operators [30], the evaluation of the Stokeslet and Stresslet is reduced to

$$G_{ij}(\mathbf{x} - \mathbf{y}) = \left(\delta_{ij} - (x_i - y_j) \frac{\partial}{\partial x_i} \right) \frac{1}{|\mathbf{x} - \mathbf{y}|} \tag{16}$$

$$\begin{aligned} T_{ijk}(\mathbf{x} - \mathbf{y}) n_k(\mathbf{x}) = \frac{1}{6} \Bigg[&\left(\delta_{ij} - (x_i - y_j) \frac{\partial}{\partial x_i} \right) \frac{\mathbf{n} \cdot (\mathbf{x} - \mathbf{y})}{|\mathbf{x} - \mathbf{y}|^3} \\ &+ \left(\delta_{ik} - (x_k - y_k) \frac{\partial}{\partial x_i} \right) \frac{n_k (x_j - y_j)}{|\mathbf{x} - \mathbf{y}|^3} \Bigg] \end{aligned} \tag{17}$$

The boundary elements involved in system of Eq. (10) are classified in a spatial tree structure in which aggregations of sources cluster together into *cells* at successive levels of refinement (see Fig. 4). The field evaluation is approximated

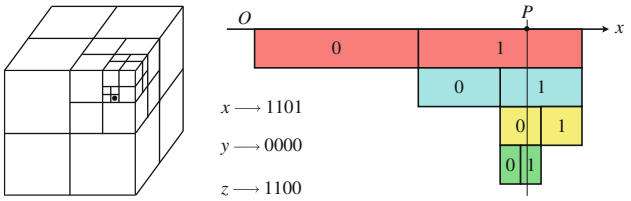

Fig. 5 Coordinates are stored as a binary keys encoding what side of the bisection and at what level the particle is located. The three coordinates are further interleaved and prepended a most significant bit. For the example shown the binary key would be $k_2 = 1\,101\,101\,000\,100$ which translates to the decimal integer $k_{10} = 6\,980$

through a tree traversal that is truncated according to a prescribed numerical tolerance ϵ. Knowing the maximum distance of the particles from the centre of the cell d, and the value of the correspondent quadrupole moment B_2, for expansions up to second order, an analytical expression for the error per interaction can be derived [32]

$$r = \frac{d}{2} + \sqrt{\frac{d^2}{4} + \sqrt{\frac{3B_2}{\epsilon}}} \tag{18}$$

leading to a strict criteria defining the smallest interaction distance r to be considered for each cell. This efficiently truncates the calculation by clearly establishing how much the algorithm must traverse the hierarchical structure to obtain the desired precision.[2]

BEM- EARTH uses a hashed octtree method to hierarchically partition 3D space and store cell locations in a integer key. A point P with coordinates $\mathbf{x} = (x, y, z)$ point is located by iteratively bisecting the volume at each axis and storing a single bit representing that it is to be found to the left (0) or right (1) of the midpoint (see Fig. 5). Resulting coordinate words are bitwise interleaved and prepended with a 1-bit to represent all nodes at each level consistently without ambiguities derived from trailing zeroes:

$$\begin{array}{c|c|ccc|ccc|ccc|ccc} x & & 1 & & & 1 & & & 0 & & & 1 & & \\ y & & & 0 & & & 0 & & & 0 & & & 0 & \\ z & & & & 1 & & & 1 & & & 0 & & & 0 \\ k_2 & 1 & 1 & 0 & 1 & 1 & 0 & 1 & 0 & 0 & 0 & 1 & 0 & 0 \end{array}$$

This key is directly mapped to index memory locations containing the cell dependent data needed for the calculation and simplifies its balanced distribution in a parallel system. The stopping criteria at each level of refinement is linked to the most significant bit.

A parallel generalised minimal residual method with restart parameter k is used to iteratively solve Eq. (10). Once the flow field at the surfaces is known, an explicit second

[2] Similar truncation of matrix entries can be achieved by the wavelet method [29], albeit with a more complicated strategy where its polynomial order depends on the scale.

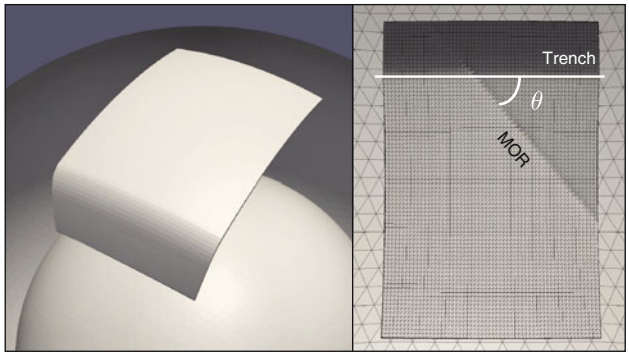

Fig. 6 Typical model setup

order Runge–Kutta adaptive timestep integration of Eq. (9) is performed. The solution is thus only calculated at the end of step and at the half-step. The time step size is constrained by a maximum displacement parameter smaller than half of the characteristic length of the smallest element, satisfying the convergence criteria of the solver. An incompressibility condition is enforced a posteriori on each surface by comparing the total volume surrounded by each interface with the previous timestep, and isotropically correcting the normal displacements according to the residual found. The thin lubrication layer is implemented through an additional correction of normal stresses of the surface elements that lie within a fixed distance of the external surface [18,19].

As the surfaces to be studied have a constrained size and their evolution is followed only up to the point where reach the core-mantle boundary, the deformation of the mesh is not significant enough to require remeshing or additional algorithms to prevent topological changes.

Each model consisting of 61,260 elements with 30,636 nodes was run on a single 8-core SGI Altix XE310 Server blade containing two Intel Xeon X5355 2.66 GHz cpus and 16 GB RAM, part of the Silica cluster at The University of Sydney. The models ran for 150 timesteps with an average 310 s cpu time per step for a total of 13 h of cpu time per run, equivalent to about an hour and a half real time per model. Overall, the useful work performed by BEM- EARTH scales as $\mathcal{O}(N \log N)$ for N boundary elements [21].

5 Oblique ridge subduction model

The different impermeable viscosity/density contrasts defining the phases are the plate surface, the core-mantle boundary and the surface of the Earth, which is free to deform under the stresses produced by the underlying lithosphere and mantle, and has a thin lubrication layer underneath.

We model a rectangular plate with fixed width and length and a thickness of 95 km immersed in a non layered homogeneous mantle and impose density and viscosity contrasts at its boundary (see Fig. 6). The lithosphere is taken to be

Table 1 Basic model parameters

Density (contrast)		
Mantle	ρ_{M}	$3,300\ \mathrm{kg\ m^{-3}}$
Lithosphere	$\Delta\rho$	$30\ \mathrm{kg\ m^{-3}}$
Viscosity		
Mantle	μ_0	1.0×10^{21} Pa s
Lithosphere	μ	200.0×10^{21} Pa s
Core	μ_{C}	10.0×10^{21} Pa s
Gravity (magnitude)	g	$10\ \mathrm{ms}^2$
Plate dimensions	$L \times W \times D$	$5{,}097 \times 3{,}823 \times 95\ \mathrm{km}^3$

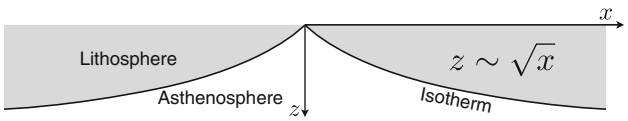

Fig. 7 Profile of a mid ocean ridge

200 times more viscous and than its surrounding mantle, and having a constant density contrast of $\Delta\rho = 30\ \mathrm{kgm}^{-3}$ respect to it. The plate is initially discretised as a regular triangular mesh subdivided 80, 60 and 4 times along its length, width and depth respectively, with a minimum initial mesh element length of around 20 km requiring a total of circa 90,000 boundary elements. As the simulation progresses, the mesh deforms into an unstructured mesh with variable resolution. Though it is possible to adaptively remesh the surface in response to changes in curvature, we chose not to in favour of computational efficiency. The basic model parameters are shown in Table 1. The plate is indented according to the lithospheric thickness profile of a MOR which follows a linear relationship between the thickness off the lithosphere and the square root of the normal distance to the axis (see Fig. 7). Once indented, the plate is bent at a dipping angle of 50° to represent ongoing subduction of 15 % of its length when the simulation starts. The shape is projected to the sphere according to its thickness and depth and positioned in between the surfaces representing the core and surface of the Earth. Similar setups for which the angle θ between the MOR axis and the trench is varied between 0° and 90° are studied.

6 Results

The BEM- EARTH code approximation leads to a very coherent plate motion typical of viscous slab numerical and laboratory experiments on subduction [3,28]. All model runs experience a transition stage in which the surface of the Earth deforms as the lubrication layer responds to lithostatic compensation. The system then evolves freely under the influence of gravity through slab pull, until it reaches a quasi-steady-state regime in which plate motion increases very gradually

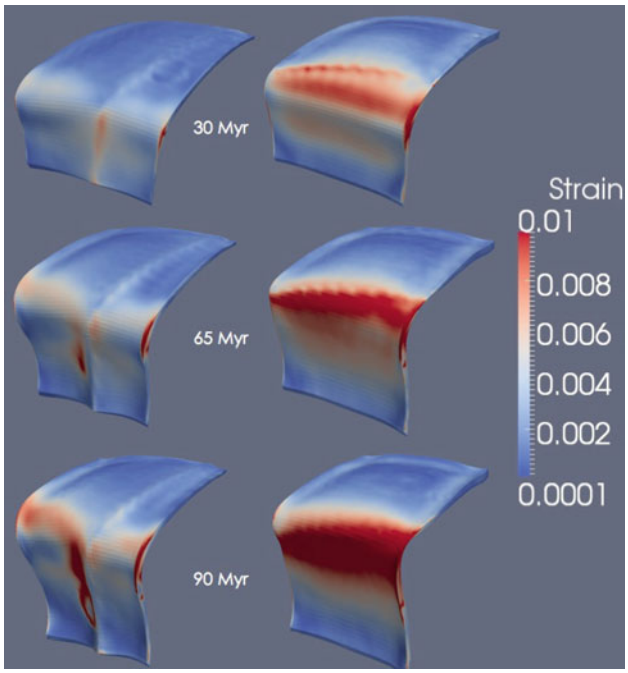

Fig. 8 Time evolution of oblique MOR subduction at 80° (*left*) and 10° (*right*) after 30, 65 and 90 million years

in time and the slab subducts in a near vertical fashion. It is in this stage that the different modes of subduction depending on the oblique MOR angle become apparent. Finally the slab reaches the core and the simulation stops.

Throughout the runs the strain rates at the tail of the plate are consistently low for all the models and only a small degree of lateral subduction and shortening is to be noticed as a boundary effect. In general most of the strain accumulates in the bending of the trench and around the MOR axis, but as subduction progresses the onset of two different modes of subduction are to be noticed (see Fig. 8). Varying the angle between the MOR axis and the trench results in two distinctive phases of subduction dynamics whose end members are characterised by compression and folding in one case and pure stretching and necking in the other (see Fig. 9).

In the first case the slab accommodates to the reduced space available at depth with a sharp fold localised around the near-vertical MOR axis and presents a very uniform inward radial speed or *sinking rate*. In contrast, near parallel to trench subduction of a MOR shows a strong differential sinking rate between each side of the ridge and a high strain rate spread over a broader region around both trench and ridge axis. A transition between these two regimes is to be found at around 60° when the sinking rates at both sides of the MOR becomes comparable (see Fig. 10). The relative motion of points at different sides of the ridge indicates that the two resulting regimes are further distinguished by a compressive versus an extensional regime across the ridge.

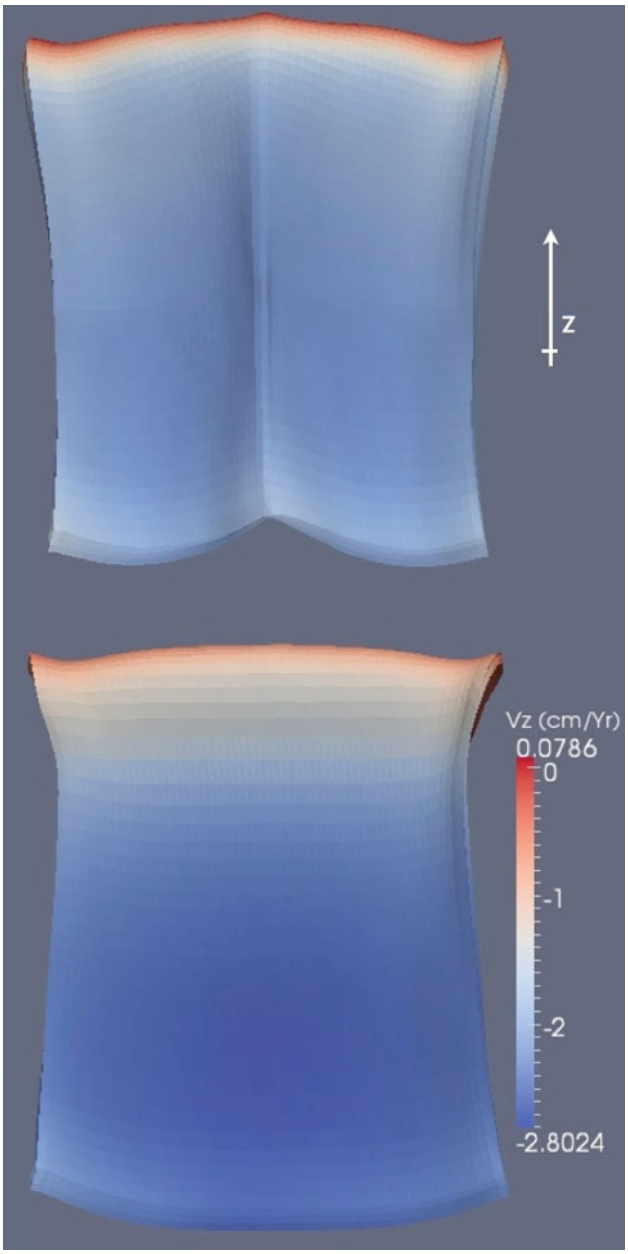

Fig. 9 MOR subduction orthogonal (*top*) and parallel to the trench (*bottom*) as end members of oblique MOR subduction dynamics characterised by folding and by necking and stretching respectively. (Color figure online)

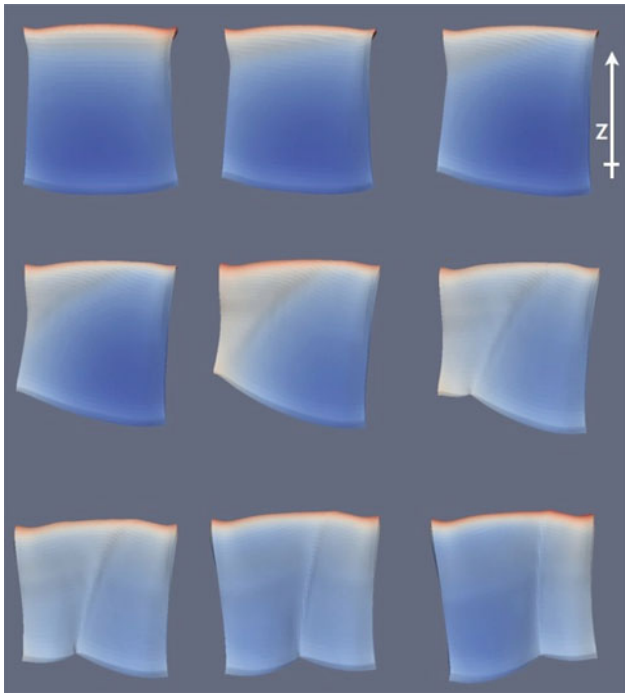

Fig. 10 Slabs of increasing oblique subduction angle from 0° to 80° in 10° increments, *coloured* according to their sinking rates (v_z) as in Fig. 9. The *first element in the last row* is the 60° critical angle for which the sinking rates at both sides are comparable

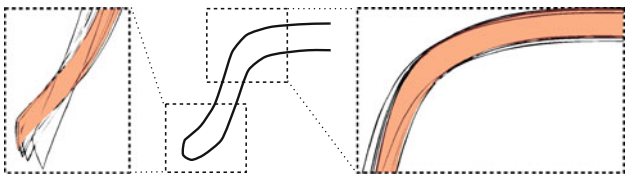

Fig. 11 Change in shape of the subducting slab after 100 timesteps with varying resolution. As resolution increases the profile approaches the shaded region, suggesting convergence (cf. [19])

We have tested a the robustness of the results respect to the mesh resolution for a non indented square slab with a length equivalent to the radius of the Earth R_{Earth} by varying the element size between $0.005 \times R_{\text{Earth}}$ and $0.013 \times R_{\text{Earth}}$ (see Fig. 11) leading to surface meshes with a total number of elements between 5,625 and 40,000. The magnitude of the correction after 100 timesteps progressively decays at higher resolution suggesting convergence. Higher resolution models tend to be more flexible, yet the position of the trailing edge of the slab and the speed of its motion remains essentially unchanged [19].

7 Discussion and conclusions

The most remarkable result is the observation that the angle between the MOR axis and the trench seems to be related *ceteris paribus* with the two different modes of subduction which are separated at a value of around 60°. This suggests that the the oblique angle of subduction is a quantity that could control when a slab detaches forming a window or folding into a tighter closed configuration. Further numerical modelling including non-linear viscous and plastic rheology would be necessary to address this claim. Possible geological evidence could derive from the geochemical signature of

volcanism associated with slab windows in the near-parallel oblique subduction case.

In contrast to models with mantle layering, our slab sinks radially with little trench retreat until it reaches the core. Though such scenario may not be entirely realistic, it enhances the effects of oblique subduction. The fact that the stretching and folding start just after the equilibration stage at the beginning of the simulation is strong indication that the different subduction modes we have shown are likely to be present in a more detailed model including the effects of mantle layering.

Acknowledgements The authors would like to thank the Australian Research Council for financial support through the Discovery Project (DP0986377). G.M. thanks the Swiss National Science Foundation (Advanced Researcher Fellowship PA0022-121475) and the Korean government (MEST, No. 2009-0092790) for financial support. R.D.M. thanks the Australian Research Council for financial support (Laureate Fellowship). We are thankful to T. Landgrebe, C. Heine, M. Seton, N. Flament, S. Zahirovic and G. Shepherd for fruitful discussions.

References

1. Andrews ER, Billen MI (2009) Rheologic controls on the dynamics of slab detachment. Tectonophysics 464(1–4):60–69
2. Barnes J, Hut P (1986) A hierarchical o(n log n) force-calculation algorithm. Nature 324(4):446–449
3. Bellahsen N, Faccenna C, Funiciello F (2005) Dynamics of subduction and plate motion in laboratory experiments: insights into the "plate tectonics" behavior of the earth. J Geophys Res 110(B1):1–15
4. Bird P (2003) An updated digital model of plate boundaries. Geochem Geophys Geosyst 4(3):1027–1028
5. Burkett ER, Billen MI (2009) Dynamics and implications of slab detachment due to ridge-trench collision. J Geophys Res 114(B12)
6. Burkett ER, Billen MI (2010) Three-dimensionality of slab detachment due to ridge-trench collision: laterally simultaneous boudinage versus tear propagation. Geochem Geophys Geosyst 11(11)
7. Cheng H, Greengard L, Rokhlin V (1999) A fast adaptive multipole algorithm in three dimensions. J Comput Phys 155(2):468–498
8. Cloos M (1993) Lithospheric buoyancy and collisional orogenesis: Subduction of oceanic plateaus, continental margins, island arcs, spreading ridges, and seamounts. Geol Soc Am Bull 105(6):715–737
9. Conrad CP, Lithgow-Bertelloni C (2002) How mantle slabs drive plate tectonics. Science 298(5591):207–209
10. Conrad CP, Lithgow-Bertelloni C (2004) The temporal evolution of plate driving forces: Importance of "slab suction" versus "slab pull" during the cenozoic. J Geophys Res 109(B10)
11. Gerya T (2011) Future directions in subduction modeling. J Geodyn 52(5):344–378
12. Gerya TV, Yuen DA, Maresch WV (2004) Thermomechanical modelling of slab detachment. Earth Planet Sci Lett 226(1–2):101–116
13. Greengard L, Rokhlin V (1987) A fast algorithm for particle simulations. J Comput Phys 73(2):325–348
14. Groome W, Thorkelson D (2009) The three-dimensional thermomechanical signature of ridge subduction and slab window migration. Tectonophysics 464(1-4):70–83
15. Hager BH, O'Connell RJ (1981) A simple global model of plate dynamics and mantle convection. J Geophys Res 86(B6):4843–4867
16. Ingber M, Mondy L (1993) Direct second kind boundary integral formulation for stokes flow problems. Comput Mech 11(1):11–27
17. Morra G, Chatelain P, Tackley P, Koumoutsakos P (2007) Large scale three-dimensional boundary element simulation of subduction. In: Shi Y, van Albada GD, Dongarra J, Sloot PM (eds) Computational Science (ICCS 2007) 7th international conference, Beijing, China, May 27–30, 2007, Proceedings, Part I. Lecture notes in computer science, vol 4489, Springer, Heidelberg, pp 1122–1129
18. Morra G, Chatelain P, Tackley P, Koumoutsakos P (2009) Earth curvature effects on subduction morphology: modeling subduction in a spherical setting. Acta Geotech 4(2):95–105
19. Morra G, Quevedo L, Müller RD (2012) Spherical dynamic models of top-down tectonics. Geochem Geophys Geosyst 13
20. Morra G, Regenauer-Lieb K, Giardini D (2006) Curvature of oceanic arcs. Geology 34(10):877–880
21. Morra G, Yuen DA, Boschi L, Chatelain P, Koumoutsakos P, Tackley PJ (2010) The fate of the slabs interacting with a density/viscosity hill in the mid-mantle. Phys Earth Planet Inter 180(3–4):271–282
22. OzBench M, Regenauer-Lieb K, Stegman DR, Morra G, Farrington R, Hale A, May DA, Freeman J, Bourgouin L, Mühlhaus H, Moresi L (2008) A model comparison study of large-scale mantle-lithosphere dynamics driven by subduction. Phys Earth Planet Inter 171(1–4):224–234
23. Pozrikidis C (1992) Boundary integral and singularity methods for linearized viscous flow, vol 7. Cambridge University Press, Cambridge
24. Quevedo L, Morra G, Müller RD (2010) Parallel fast multipole boundary element method for crustal dynamics. IOP Conf Ser Mater Sci Eng 10(1):012
25. Ribe N (2010) Bending mechanics and mode selection in free subduction: a thin-sheet analysis. Geophys J Int 180(2):559–576
26. Salvadori A (2001) Analytical integrations of hypersingular kernel in 3d bem problems. Comput Methods Appl Mech Eng 190(31):3957–3975
27. Shen L, Liu Y (2007) An adaptive fast multipole boundary element method for three-dimensional potential problems. Comput Mech 39(6):681–691
28. Stegman DR, Freeman J, Schellart WP, Moresi L, May D (2006) Influence of trench width on subduction hinge retreat rates in 3-d models of slab rollback. Geochem Geophys Geosyst 7(3)
29. Tausch J (2003) Sparse BEM for potential theory and stokes flow using variable order wavelets. Comput Mech 32(4):312–318
30. Tornberg AK, Greengard L (2008) A fast multipole method for the three-dimensional stokes equations. J Comput Phys 227(3):1613–1619
31. Turcotte DL, Schubert G (2002) Geodynamics, vol 2. Cambridge University Press, Cambridge
32. Warren MS, Salmon JK (1993) A parallel hashed oct-tree n-body algorithm. In: Borchers B, Crawford D (eds) Supercomputing 93: Proceedings of the 1993 ACM/IEEE conference on supercomputing. ACM, New York, pp 12–21
33. Whittaker JM, Müller RD, Leitchenkov G, Stagg H, Sdrolias M, Gaina C, Goncharov A (2007) Major australian-antarctic plate reorganization at hawaiian-emperor bend time. Science 318(5847):83–86
34. Zhu G, Mammoli A, Power H (2006) A 3-d indirect boundary element method for bounded creeping flow of drops. Eng Anal Bound Elem 30(10):856–868